Astronomy
&
Astrophysics

Cosmology with gamma-ray bursts

I. The Hubble diagram through the calibrated $E_{p,i}$–E_{iso} correlation

Marek Demianski[1,2], Ester Piedipalumbo[3,4], Disha Sawant[5,6], and Lorenzo Amati[7]

[1] Institute for Theoretical Physics, University of Warsaw, Pasteura 5, 02-093 Warsaw, Poland
[2] Department of Astronomy, Williams College, Williamstown, MA 01267, USA
[3] Dipartimento di Fisica, Università degli Studi di Napoli Federico II, Compl. Univ. Monte S. Angelo, 80126 Napoli, Italy
e-mail: ester@na.infn.it
[4] I.N.F.N., Sez. di Napoli, Compl. Univ. Monte S. Angelo, Edificio 6, via Cinthia, 80126 Napoli, Italy
[5] Dipartimento di Fisica e Scienze della Terra, Università degli Studi di Ferrara, 44121 Ferrara, Italy
[6] Department of Physics, University of Nice Sophia Antipolis, Parc Valrose, 06034 Nice Cedex 2, France
[7] INAF–IASF, Sezione di Bologna, via Gobetti 101, 40129 Bologna, Italy

ABSTRACT

Context. Gamma-ray bursts (GRBs) are the most energetics explosions in the Universe. They are detectable up to very high redshifts. They may therefore be used to study the expansion rate of the Universe and to investigate the observational properties of dark energy, provided that empirical correlations between spectral and intensity properties are appropriately calibrated.

Aims. We used the type Ia supernova (SN) luminosity distances to calibrate the correlation between the peak photon energy, $E_{p,i}$, and the isotropic equivalent radiated energy, E_{iso} in GRBs. With this correlation, we tested the reliability of applying these phenomena to measure cosmological parameters and to obtain indications on the basic properties and evolution of dark energy.

Methods. Using 162 GRBs with measured redshifts and spectra as of the end of 2013, we applied a local regression technique to calibrate the $E_{p,i}$–E_{iso} correlation against the type Ia SN data to build a calibrated GRB Hubble diagram. We tested the possible redshift dependence of the correlation and its effect on the Hubble diagram. Finally, we used the GRB Hubble diagram to investigate the dark energy equation of state (EOS). To accomplish this, we focused on the so-called Chevalier-Polarski-Linder (CPL) parametrization of the dark energy EOS and implemented the Markov chain Monte Carlo (MCMC) method to efficiently sample the space of cosmological parameters.

Results. Our analysis shows once more that the $E_{p,i}$–E_{iso} correlation has no significant redshift dependence. Therefore the high-redshift GRBs can be used as a cosmological tool to determine the basic cosmological parameters and to test different models of dark energy in the redshift region ($z \geqslant 3$), which is unexplored by the SNIa and baryonic acoustic oscillations data. Our updated calibrated Hubble diagram of GRBs provides some marginal indication (at 1σ level) of an evolving dark energy EOS. A significant enlargement of the GRB sample and improvements in the accuracy of the standardization procedure is needed to confirm or reject, in combination with forthcoming measurements of other cosmological probes, this intriguing and potentially very relevant indication.

Key words. cosmological parameters – dark energy – cosmology: theory

1. Introduction

Starting at the end of the 1990s, observations of high-redshift supernovae of type Ia (SNIa) revealed that the Universe is now expanding at an accelerated rate (see e.g. Perlmutter et al. 1998, 1999; Riess et al. 1998, 2007; Schmidt et al. 1998; Astier et al. 2006; Amanullah et al. 2010). This surprising result has been independently confirmed by statistical analyses of observations of small-scale temperature anisotropies of the cosmic microwave background (CMB) radiation Spergel et al. (2007), Planck Collaboration XVI (2014), Planck Collaboration XIII (2016). It is usually assumed that the observed accelerated expansion is caused by the so-called dark energy, a cosmic medium with unusual properties. The pressure of dark energy p_{de} is negative and is related to the positive energy density of dark energy ϵ_{de} by $p_{de} = w \epsilon_{de}$, where the proportionality coefficient, that is, the equation of state (EOS), w, is negative ($w < -1/3$). According to current estimates, about 70% of the matter energy in the Universe is in the form of dark energy, so

that today dark energy is the dominant component in the Universe. The nature of dark energy is, however, not known. The models of dark energy proposed so far can be divided into at least three groups: a) a non-zero cosmological constant (see for instance Carroll 2001), in this case $w = -1$, b) a potential energy of some not yet discovered scalar field (see for instance Sahni et al. 2003; Alam et al. 2003), or c) effects connected with the inhomogeneous distribution of matter and averaging procedures (see for instance Clarkson & Maartens 2010). In the last two cases, in general, $w \neq -1$ and is not constant, but depends on the redshift z. To test whether and how w changes with redshift, it is necessary to use more distant objects. It is commonly argued that since the dark energy density term becomes subdominant (with respect to the dark matter) at $z \gtrsim 0.5$ Riess et al. (2004), it is not important to study its EOS at earlier epochs. However, this argument is unreliable: even within the simplest model, the dark energy contributes nearly $\simeq 10\%$ of the overall cosmic energy density at $z \simeq 2$ and strongly alters the deceleration parameter with the cosmological constant. Moreover, for several observables the

Fig. 2. Redshift distribution of our sample of 162 long GRBs/XRFs and the Union 2.1 SNIa dataset.
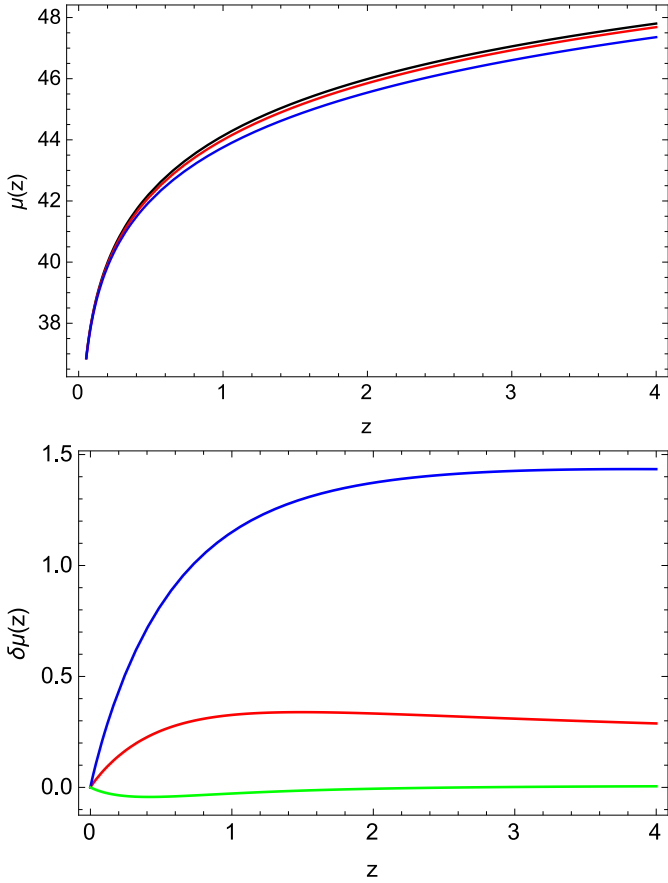
Fig. 1. Dependence of the distance modulus on EOS of dark energy. *Upper panel*: distance modulus $\mu(z)$ for different values of the EOS parameters. The black line represents the standard flat ΛCDM model with $\Omega_m = 0.3$, $h = 0.7$, $w_0 = -1$, $w_1 = 0$. The other curves correspond to different values of the CPL parameters w_0 and w_1. *Bottom panel*: z dependence of the percentage error in the distance modulus between the fiducial ΛCDM model and different flat CPL models, as in the left panel.

sensitivity to the dark energy equation of state increases at high redshifts. In Fig. 1 we explore this aspect following a simplified approach, considering the modulus of distance $\mu(z)$ as observable: we fixed a flat Λ cold dark matter (ΛCDM) fiducial cosmological model, constructing the corresponding $\mu_{fid}(z, \theta)$, and plot the percentage error on the distance modulus with respect to different corresponding functions evaluated in the framework of a flat CPL quintessence model Chevallier & Polarski (2001), Linder (2003). We selected $\Omega_m = 0.3$ and $h = 0.7$ and varied the dark EOS parameters w_0 and w_1. It is worth noting that a higher sensitivity is reached only for $z \gtrsim 2$. Therefore, investigating the cosmic expansion of the Universe also beyond these redshifts remains a fundamental probe of dark energy. In this scenario, new possibilities opened up when gamma-ray bursts (GRBs) were discovered at higher redshifts. The current record is at $z = 9.4$ (Tanvir et al. 2009; Salvaterra et al. 2009; Cucchiara 2011). It is worth noting that the photometric redshift on GRB 090429B is quite high, especially on the low side; GRB 090423, for which a spectroscopic redshift is available, is much better determined. GRBs span a redshift range better suited for probing dark energy than the SNIa range, as shown in Fig. 2, where we compare the distribution in redshift of our sample of 162 long GRBs/XRFs with the Union 2.1 SNIa dataset.

Gamma-ray bursts are enigmatic objects, however. First of all, the mechanism that is responsible for releasing the high
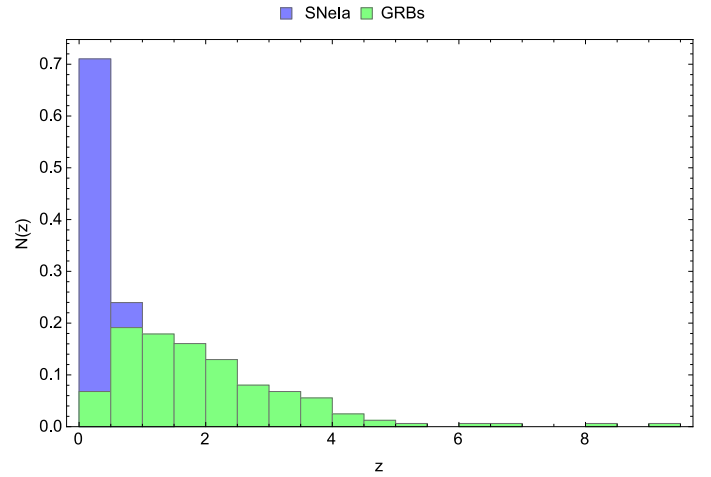
amounts of energy that a typical GRB emits is not yet completely known, and only some aspects of the progenitor models are well established, in particular that long GRBs are produced by core-collapse events, see for instance Meszaros (2006) and Vedrenne & Atteia (2009). Despite these difficulties, GRBs are promising objects for studying the expansion rate of the Universe at high redshifts. One of the most important aspects of the observational property of long GRBs is that they show several correlations between spectral and intensity properties (luminosity, radiated energy). Here we consider the correlation between the observed photon energy of the peak spectral flux, $E_{p,i}$, which corresponds to the peak in the νF_ν spectra, and the isotropic equivalent radiated energy E_{iso} (e.g., Amati et al. 2002; Amati 2006),

$$\log\left(\frac{E_{iso}}{1\,erg}\right) = b + a \log\left[\frac{E_{p,i}}{300\,keV}\right], \tag{1}$$

where a and b are constants, and $E_{p,i}$ is the spectral peak energy in the GRB cosmological rest-frame, which can be derived from the observer frame quantity, E_p, by $E_{p,i} = E_p(1 + z)$. This correlation not only provides constraints for the model of the prompt emission, but also naturally suggests that GRBs can be used as distance indicators. The isotropic equivalent energy E_{iso} can be calculated from the bolometric fluence S_{bolo} as

$$E_{iso} = 4\pi d_L^2(z, cp)S_{bolo}(1 + z)^{-1}, \tag{2}$$

where d_L is the luminosity distance and cp denotes the set of parameters that specify the background cosmological model. It is clear that to be able to use GRBs as distance indicators, it is necessary to consistently calibrate this correlation. Unfortunately, owing to the lack of GRBs at very low redshifts, the calibration of GRBs is more difficult than that of SNIa, and several calibration procedures have been proposed so far (see for instance Cardone et al. 2008; Demianski et al. 2011, 2012; Gao et al. 2012; Postnikov et al. 2014; Dai et al. 2004; Liu & Wei 2015; Lin et al. 2015). We here apply a local regression technique to determine the correlation parameters a and b, using the recently updated SNIa sample and to construct a new calibrated GRB Hubble diagram that can be used for cosmological investigations. We then use this calibrated GRB Hubble diagram to investigate the cosmological parameters through the Markov chain Monte Carlo technique (MCMC), which simultaneously computes the full posterior probability density functions of all the parameters. The structure of the paper is as follows. In

Sect. 2 we describe the methods used to fit the $E_{p,i}$–E_{iso} correlation and construct the calibrated GRB Hubble diagram. In Sect. 3 we present our cosmological constraints and investigate the possible redshift dependence and Malmquist-like bias effects. In Sect. 4, as an additional self-consistency check, we apply the Bayesian method for the non-calibrated $E_{p,i}$–E_{iso} correlation and simultaneously extract the correlation coefficients and the cosmological parameters of the model. Section 5 is devoted to the discussion of our main results and conclusions.

2. Standardizing GRBs and constructing the Hubble diagram

The GRBs νF_ν spectra are well modeled by a phenomenological smoothly broken power law, characterized by a low-energy index, α, a high-energy index, β, and a break energy E_0. They show a peak corresponding to a specific (and observable) value of the photon energy $E_p = E_0(2 + \alpha)$. For GRBs with measured spectrum and redshift it is possible to evaluate the intrinsic peak energy, $E_{p,i} = E_p(1 + z)$ and the isotropic equivalent radiated energy

$$E_{iso} = 4\pi d_L^2(z, cp)(1 + z)^{-1} \int_{1/1+z}^{10^4/1+z} EN(E)\mathrm{d}E,$$

where $N(E)$ is the Band function:

$$N(E) = \begin{cases} A\left(\frac{E}{100\,\mathrm{KeV}}\right)^\alpha \exp\left(\frac{-E}{E_0}\right) & (\alpha - \beta)\,E_0 \geq 0, \\ A\left(\frac{(\alpha-\beta)E}{100\,\mathrm{KeV}}\right)^{\alpha-\beta} \exp(\alpha - \beta)\left(\frac{E}{100\,\mathrm{KeV}}\right)^\beta & (\alpha - \beta)\,E_0 \leq E. \end{cases}$$
$$(3)$$

E_{iso} and $E_{p,i}$ span several orders of magnitude (therefore GRBs cannot be considered standard candles), and show distributions approximated by Gaussians plus a tail at low energies. A strong correlation between these two quantities was initially discovered in a small sample of Beppo SAX GRBs with known redshifts (Amati et al. 2002) and confirmed afterward by HETE-2 and *Swift* observations Lamb et al. (2005), Amati (2006). Several analyses of the $E_{p,i}$-E_{iso} plane of GRBs showed that different classes of GRBs exhibit different behaviors, and while normal long GRBs and X-ray flashes (XRF, i.e., particularly soft bursts) follow this correlation, with the exception of the two peculiar subenergetic GRBs 980425 and 031203 see, e.g., Amati et al. (2007), for a discussion on possible explanations, short GRBs do not. These facts may depend on the different emission mechanisms and/or geometry involved in different classes of GRBs and makes this correlation a useful tool to distinguish between them (Amati 2006; Antonelli et al. 2009). Although it was the first strong correlation discovered for the GRB observables, until recent years, the $E_{p,i}$–E_{iso} correlation was never used for cosmology because it exhibits a significant dispersion around the best-fit power law: the residuals follow a Gaussian with a value of $\sigma_{\log E_{p,i}} \simeq 0.2$. This type of additional Poissonian scatter is typically quantified by performing a maximum likelihood analysis that takes the variance and the errors on dependent and independent variables into account. By measuring $E_{p,i}$ in keV and E_{iso} in 10^{52} erg, this method gives $\sigma_{\log E_{p,i}} = 0.19 \pm 0.02$ (Amati et al. 2008, 2009). However, the recent increase in the efficiency of GRB discoveries combined with the fact that the $E_{p,i}$–E_{iso} correlation requires only two parameters that are directly inferred from observations (this minimizes the effects of systematics and increases the number

of GRBs that can be used) makes this correlation an interesting tool for cosmology. Despite the very large number of bursts consistent with this correlation, its physical origin is still debated. Some authors claimed that it is strongly affected by instrumental selection effects (Nakar & Piran 2005; Band & Preece 2005; Butler et al. 2007; Shahmoradi & Nemiroff 2011). However, many other studies found that such instrumental selection biases, even if they may affect the sample, cannot be responsible for the existence of the spectral-energy correlations (Ghirlanda et al. 2008; Nava et al. 2012). Moreover, a recent time-resolved spectral analysis of GRBs that were detected by the *Beppo*SAX and *Fermi* satellite showed that $E_{p,i}$ correlates with the luminosity (e.g., Ghirlanda et al. 2010; Frontera et al. 2012) and radiated energy (e.g., Basak et al. 2013) also during the temporal evolution of the bursts (and the correlation between the spectral peak energy and the evolving flux has been pointed out by, e.g., Golenetskii et al. 1983 based on Konus-WIND data). The time-resolved $E_{p,i}$-luminosity and $E_{p,i}$–E_{iso} correlations within individual GRBs and that their average slope is consistent with that of correlations defined by the time-averaged spectral properties of different bursts strongly supports the physical origin of the $E_{p,i}$–E_{iso} correlation. It is very difficult to explain them as a selection or instrumental effect (e.g., Dichiara & Amati 2013; Basak et al. 2013), and the predominant emission mechanism in GRB prompt emission produces a correlation between the spectral peak energy and intensity (which can be characterized either as luminosity, peak luminosity, or radiated energy). In addition to its existence and slope, an important property of the $E_{p,i}$–E_{iso} correlation is its dispersion. As shown by several works that were based on the so-called jet-breaks, in the optical afterglow light curves of some GRBs (e.g., Ghirlanda et al. 2004, 2006), 50% of the extra-Poissonian scatter of the correlation is sometimes probably a result of the distribution of jet opening angles. However, these estimates of jet opening angles are still unconfirmed and model-dependent and can be made only for a small number of GRBs. Other factors that may contribute to the dispersion of the $E_{p,i}$–E_{iso} and other $E_{p,i}$-intensity correlations include the jet structure, viewing angles, detectors sensitivity, and energy band (but see Amati et al. 2009), the diversity of shock microphysics parameters, and the magnetization within the emitting ejecta. At the current observational and theoretical status, it is very difficult to quantify these single contributions, which seem to act randomly in scattering the data around the best fit power-law (e.g., Ghirlanda et al. 2008; Amati et al. 2008). Importantly, it has been shown (e.g., Amati et al. 2009) that a small fraction (5–10%) of the scatter depends on the cosmological model and parameters assumed for computing E_{iso}, which makes this correlation a potential tool for cosmology.

In this section we show how the $E_{p,i}$–E_{iso} correlation can be calibrated to standardize long GRBs and to build a GRB Hubble diagram, which we use to investigate different cosmological models at very high redshifts (see also Amati & Della Valle 2013; Wang et al. 2015, 2016; Lin et al. 2015, 2016b).

2.1. GRB data

We used a sample of 162 long GRBs/XRFs as of September 2013 taken from the updated compilation of spectral and intensity parameters of GRBs by Sawant & Amati (2016). The redshift distribution of this sample covers a broad range, $0.03 \leq z \leq 9.3$, which means that it extends far beyond the SNIa range ($z \leq 1.7$). These data are of long GRBs/XRFs that are characterized by firm measurements of redshifts and the restframe peak energy

$E_{p,i}$. The main contributions come from the joint detections by *Swift*/BAT and *Fermi*/GBM or Konus-WIND, except for the small fraction of events for which *Swift*/BAT can directly provide $E_{p,i}$ when it is in the $(15-150)$ keV interval. For events detected by more than one of these detectors, the uncertainties on the $E_{p,i}$ and E_{iso} take the measurements and uncertainties provided by each individual detector into account. In Table 4 we report for each GRB the redshift, the restframe spectral peak energy, $E_{p,i}$, and the isotropic-equivalent radiated energy, E_{iso}. As detailed in (Sawant & Amati, in prep.), the criterion behind selecting the observations from a particular mission is based on the conditions summarized below.

1. We preferred observations with exposure times of at least two-thirds of the whole event duration. Hence Konus-WIND and *Fermi*/GBM were chosen whenever available. For Konus-WIND, the observations were reported in the official literature (see e.g. Ulanov et al. 2005), and also in GCN archives when needed. For *Fermi*/GBM, the observations were taken from Gruber et al. (2012), from several other papers (e.g., Ghirlanda et al. 2004, 2005; Friedman & Bloom 2005, etc.), and from GCNs.

2. The *Swift*/BAT observations were chosen when no other preferred mission (Konus-WIND, *Fermi*/GBM) was able to provide spectral parameters and the value of $E_{p,obs}$ was within the energy band of this instrument. In particular, the $E_{p,i}$ values derived from BAT spectral analysis were conservatively taken from the results reported by the BAT team (Sakamoto et al. 2008a,b). Other BAT $E_{p,i}$ values reported in the literature were not considered because they were not confirmed by Sakamoto et al. (2008a,b), by a refined analysis (see e.g. Cabrera et al. 2007), or because they were based on speculative methods Butler et al. (2007).

When available, the Band model Band et al. (1993) was considered as the cut-off power law, which sometimes overestimates the value of $E_{p,i}$. Finally, the error on any value was assumed to be not less than 10% to account for the instrumental capabilities and calibration uncertainties.

2.2. Cosmologically independent calibration: local regression of SNIa

The lack of nearby GRBs creates the so-called circularity problem: GRBs can be used as cosmological tools through the $E_{p,i}$–E_{iso} correlation, which is based on the cosmological model assumed for the computation of E_{iso}, however. In principle, this problem could be solved in several ways: it is possible, for instance, to simultaneously constrain the calibration parameters $(a, b, \sigma_{int}) \in G$ and the set of cosmological parameters $\theta \in H$ by considering a likelihood function defined in the space $G \otimes H$, which allows simultaneously fitting the parameters (e.g., Diaferio et al. 2011). This procedure is implemented in Sect. 5 and compared with the local regression technique. Alternatively, it has been proposed that the problem might be avoided by considering a sufficiently large number of GRBs within a small redshift bin centered on any z Ghirlanda et al. (2006). However, this method, even if quite promising for the future, is currently unrealistic because of the limited number of GRBs with measured redshifts. In this section we implement a procedure for calibrating the $E_{p,i}$–E_{iso} relation in a way independent of the cosmological model by applying a local regression technique to estimate the distance modulus $\mu(z)$ from the recently updated SNIa sample, called Union2.1 (see also Kodama et al. 2008; Liang et al. 2008). Originally implemented by Cleveland & Devlin (1988),

this technique combines the simplicity of linear regression with the flexibility of nonlinear regression to localized subsets of the data, and reconstructs a function describing their behavior in the neighborhood of any point z_0. A low-degree polynomial is fitted to a subsample containing a neighborhood of z_0, by using weighted least-squares with a weight function that quickly decreases with the distance from z_0. The local regression procedure can be schematically sketched as follows:

1. set the redshift z where $\mu(z)$ has to be reconstructed;
2. sort the SNIa Union2.1 sample by increasing value of $|z - z_i|$ and select the first $n = \alpha \mathcal{N}_{SNIa}$, where α is a user-selected value and $\mathcal{N}_{SNIa}$ the total number of SNIa;
3. apply the weight function

$$W(u) = \begin{cases} (1 - |u|^2)^2 & |u| \leq 1 \\ 0 & |u| \geq 1, \end{cases} \qquad (4)$$

where $u = |z - z_i|/\Delta$ and Δ the highest value of the $|z - z_i|$ over the previously selected subset;
4. fit a first-order polynomial to the data previously selected and weighted, and use the zeroth-order term as the best-fit value of the modulus of distance $\mu(z)$;
5. evaluate the error σ_μ as the root mean square of the weighted residuals with respect to the best-fit value.

It is worth stressing that both the choice of the weight function and the order of the fitting polynomial are somewhat arbitrary. Similarly, the value of n to be used must not be too low to make up a statistically valuable sample, but also not too high to prevent the use of a low-order polynomial. To check our local regression routine, we simulated a large catalog with the same redshift and error distribution as the Union2.1 survey. We adopted a quintessence cosmological model with a constant EOS, w, and fixed values of the cosmological parameters (Ω_M, w, h). For each redshift value in the Union2.1 sample, we extracted the corresponding modulus of distance from a Gaussian distribution centered on the theoretically predicted value and with the standard deviation $\sigma = 0.15$. To this value, we added the value of the error, corresponding to the same relative uncertainty as the data in the Union sample. This simulated catalog was used as input to the local regression routine, and the reconstructed $\mu(z)$ values were compared to the input ones.

Defining the percentage deviation $\epsilon = \frac{\mu_w(z) - \mu_{rec.}(z)}{\mu_w(z)}$ with $\mu_{rec.}$ and μ_w the local regression estimate and the input values, respectively, and averaging over 500 simulations, we found that the choice $\alpha = 0.02$ gives $(\delta\mu/\mu)_{rms} \simeq 0.3\%$ with $|\epsilon| \leq 1\%$ independently on the redshift z. This result implies that the local regression method allows correctly reconstructing the underlying distance modulus regardless of redshift $z < 1.4$ from the Union SNIa sample. We also tested this results in different cosmological backgrounds by adopting an evolving EOS and averaging over five realizations of the mock catalog. With this efficient way of estimating $\mu(z)$ at redshift z in a model-independent way, we can now fit the $E_{p,i}$–E_{iso} correlation relation, using the reconstructed $\mu(z)$. We considered only GRBs with $z \leq 1.414$ to cover the same redshift range as is spanned by the SNIa data. To standardize the $E_{p,i}$–E_{iso} relation as expressed by Eq. (1), we need to fit a data array $\{x_i, y_i\}$ with uncertainties $\{\sigma_{x,i}, \sigma_{y,i}\}$, to a straight line

$$y = b + ax, \qquad (5)$$

and determine the parameters (a, b). We expect a certain amount of intrinsic additional Poissonian scatter, σ_{int}, around the best-fit
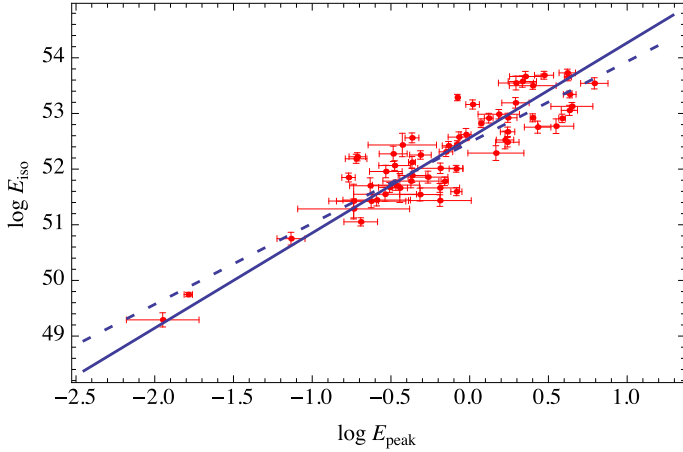
Fig. 3. Best-fit curves for the $E_{p,i}-E_{iso}$ correlation relation superimposed on the data. The solid and dashed lines refer to the results obtained with the maximum likelihood (Reichart likelihood) and weighted χ^2 estimator, respectively.

line that has to be taken into account and determined together with (a, b) by the fitting procedure. We used a likelihood, implemented by Reichart et al. (2001), that solved this problem of fitting data that are affected by extrinsic scatter in addition to the intrinsic uncertainties along both axes:

$$L_{Reichart}(a, b, \sigma_{int}) = \frac{1}{2} \frac{\sum \log (\sigma_{int}^2 + \sigma_{y_i}^2 + a^2 \sigma_{x_i}^2)}{\log (1 + a^2)}$$
$$+ \frac{1}{2} \sum \frac{(y_i - ax_i - b)^2}{\sigma_{int}^2 + \sigma_{x_i}^2 + a^2 \sigma_{x_i}^2}, \quad (6)$$

where the sum is over the $\mathcal{N}$ objects in the sample. We note that this maximization was performed in the two-parameter space (a, σ_{int}) since b may be calculated analytically by solving the equation $\frac{\partial}{\partial b} L(a, b, \sigma_{int}) = 0$, we obtained

$$b = \left[\sum \frac{y_i - ax_i}{\sigma_{int}^2 + \sigma_{y_i}^2 + a^2 \sigma_{x_i}^2} \right] \left[\sum \frac{1}{\sigma_{int}^2 + \sigma_{y_i}^2 + a^2 \sigma_{x_i}^2} \right]^{-1}. \quad (7)$$

To quantitatively estimate the goodness of this fit, we used the median and root mean square of the best-fit residuals, defined as $\delta = y_{obs} - y_{fit}$. To quantify the uncertainties of some fit parameter p_i, we evaluated the marginalized likelihood $\mathcal{L}_i(p_i)$ by integrating over the other parameters. The median value for the parameter p_i was then found by solving

$$\int_{p_{i,min}}^{p_{i,med}} \mathcal{L}_i(p_i) dp_i = \frac{1}{2} \int_{p_{i,min}}^{p_{i,max}} \mathcal{L}_i(p_i) dp_i. \quad (8)$$

The 68% (95%) confidence range $(p_{i,l}, p_{i,h})$ was then found by solving e.g., D'Agostini (2005)

$$\int_{p_{i,l}}^{p_{i,med}} \mathcal{L}_i(p_i) dp_i = \frac{1 - \varepsilon}{2} \int_{p_{i,min}}^{p_{i,max}} \mathcal{L}_i(p_i) dp_i \quad (9)$$

with $\varepsilon = 0.68$ and $\varepsilon = 0.95$ for the 68% and 95% confidence level. The maximum likelihood values of a and σ_{int} are $a = 1.75^{+0.18}_{-0.16}$ and $\sigma_{int} = 0.37^{+0.07}_{-0.08}$. In Fig. 3 we show the correlation $\log E_{p,i} - \log E_{iso}$. The solid line is the best fit obtained using the Reichart likelihood, and the dashed line is the best fit obtained by the weighted χ^2 method. The marginalized likelihood functions are shown in Fig. 4.
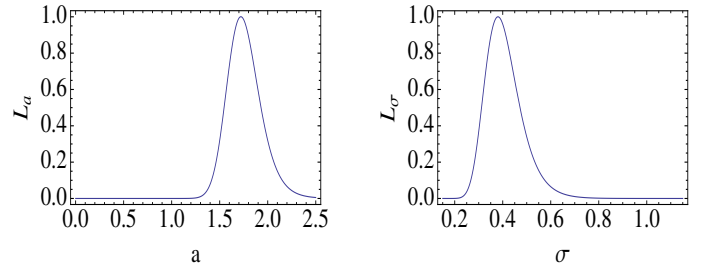

Fig. 4. Marginalized likelihood functions: the likelihood function $\mathcal{L}_a$ is obtained by marginalizing over σ_{int}; and the likelihood function, $\mathcal{L}_{\sigma_{int}}$, is obtained by marginalizing over a.
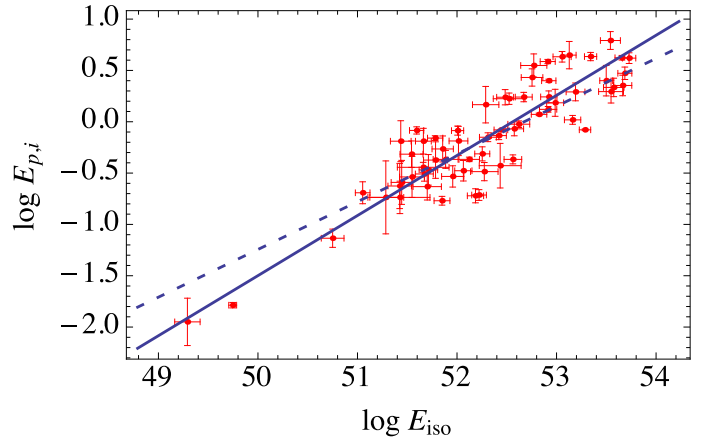

Fig. 5. Best-fit curves for the $E_{iso}-E_{p,i}$ correlation relation superimposed on the data. The solid and dashed lines refer to the results obtained with the maximum likelihood (Reichart likelihood) and weighted χ^2 estimator, respectively.

As noted above, b can be evaluated analytically. We obtained $b = 52.53 \pm 0.02$. It is worth noting that in the literature results for the inverse correlation are commonly reported, that is, the correlation $E_{iso}-E_{p,i}$: using the local regression technique and the Reichart likelihood, we also obtained this inverse calibration. We obtained $a^{inverse} = 0.58^{+0.07}_{-0.05}$, $\sigma_{int}^{inverse} = 0.24^{+0.04}_{0.03}$. In Fig. 5 we plot the best-fit curves for the $E_{iso}-E_{p,i}$ correlation relation superimposed on the data.

2.2.1. Constructing the Hubble diagram

After fitting the correlation and estimating its parameters, we used them to construct the GRB Hubble diagram. We recall that the luminosity distance of a GRB with the redshift z may be computed as

$$d_L(z) = \left(\frac{E_{iso}(1 + z)}{4\pi S_{bolo}} \right)^{1/2}. \quad (10)$$

The uncertainty of $d_L(z)$ was then estimated through the propagation of the measurement errors on the involved quantities. In particular, recalling that our correlation relation can be written as a linear relation, as in Eq. (5), where $y = E_{iso}$ is the distance dependent quantity, while x is not, the error on the distance dependent quantity y was estimated as

$$\sigma(y) = \sqrt{a^2 \sigma_x^2 + \sigma_a^2 x^2 + \sigma_b^2 + \sigma_{int}^2}, \quad (11)$$

where σ_b is properly evaluated through the Eq. (27), which implicitly defines b as a function of a and σ_{int}, and is then added
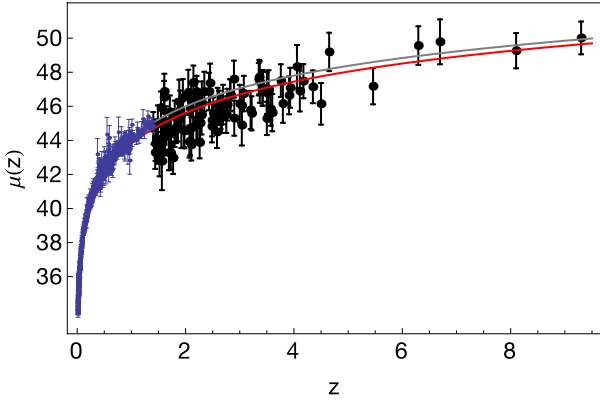
Fig. 6. Calibrated GRB Hubble diagram (black filled diamond) up to very high values of redshift, as constructed by applying the local regression technique with the Reichart likelihood: we show overplotted the behavior of the theoretical distance modulus $\mu(z) = 25 + 5 \log d_L(z)$ corresponding to the favored fitted CPL model (red line), with $w_0 = -0.29$, $w_1 = -0.12$, $h = 0.74$, $\Omega_m = 0.24$, and the standard ΛCDM model (gray line) with $\Omega_m = 0.33$, and $h = 0.74$. They are defined by Eqs. (12) and (21). The blue filled points at lower redshift are the SNIa data.
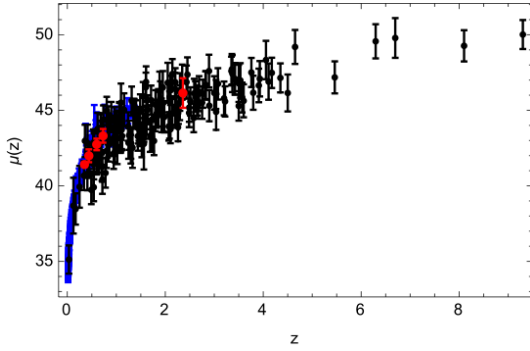

Fig. 7. GRB Hubble diagram (black points) is compared with the SNIa Hubble diagram (blue points) and with BAO data (red points).

in quadrature to the uncertainties of the other terms entering Eq. (10) to obtain the total uncertainty. The distance modulus $\mu(z)$ is easily obtained from its standard definition

$$\mu(z) = 25 + 5 \log d_L(z), \tag{12}$$

with its uncertainty obtained again by error propagation:

$$\sigma_\mu^2 = \left(\frac{5}{2}\sigma^2(y)\right)^2 + \left(\frac{5}{2\ln 10}\frac{\sigma_{S_{\text{bolo}}}}{S_{\text{bolo}}}\right)^2. \tag{13}$$

We finally estimated the distance modulus for each ith GRB in the sample at redshift z_i to build the Hubble diagram plotted in Fig. 6. We refer to this data set as the calibrated GRB Hubble diagram below since to compute the distances Hubble diagram we relied on the calibration based on the SNIa Hubble diagram. The derived distance moduli are divided into two subsets, listed in Tables 4 and 5. Table 4 lists GRBs with $z \leq 1.46$, the same redshift range as for known SNIa, and Table 5 lists GRBs with $z \geq 1.47$. In Fig. 7 we finally compare the GRB Hubble diagram (black points) with the SNIa Hubble diagram (blue points) and with BAO data (red points).

3. Cosmological constraints derived from the calibrated GRB Hubble diagram

Here we illustrate the possibilities of using the GRB Hubble diagram to constrain the cosmological models and investigate the dark energy EOS. Within the standard homogeneous and isotropic cosmology, the dark energy appears in the Friedman equations:

$$\frac{\ddot{a}}{a} = -\frac{4\pi G}{3}\left(\rho_M + \rho_{de} + 3p_{de}\right), \tag{14}$$

$$H^2 + \frac{k}{a^2} = \frac{8\pi G}{3}(\rho_M + \rho_{de}), \tag{15}$$

where a is the scale factor, $H = \dot{a}/a$ the Hubble parameter, ρ_M the density of matter, ρ_{de} the density of dark energy, p_{de} its pressure, and the dot denotes the time derivative. The continuity equation for any component of the cosmological fluid is

$$\frac{\dot{\rho}_i}{\rho_i} = -3H\left(1 + \frac{p_i}{\rho_i}\right) = -3H\left[1 + w_i(t)\right], \tag{16}$$

where the energy density is ρ_i, the pressure p_i, and the EOS of the ith component is defined by $w_i = \dfrac{p_i}{\rho_i}$. The standard non-relativistic matter has $w = 0$, and the cosmological constant has $w = -1$. The dark energy EOS and other constituents of the Universe determine the Hubble function $H(z)$ and any derivations of it that are needed to obtain the observable quantities. When only matter and dark energy are present, the Hubble function is given by

$$H(z,\theta) = H_0\sqrt{(1 - \Omega_m)g(z,\theta) + \Omega_m(z+1)^3 + \Omega_k(z+1)^2}, \tag{17}$$

where $g(z) = \exp(3\int_0^z \frac{w(x,\theta) + 1}{x+1}\,dx)$, and $w(z,\theta)$ describes the dark energy EOS, characterized by n parameters $\theta = (\theta_1, \theta_2, ..., \theta_n)$. We limit our analysis below to the CPL parametrization,

$$w(z) = w_0 + w_1 z(1+z)^{-1}, \tag{18}$$

where w_0 and w_1 are constant parameters and they represent the $w(z)$ present value and its overall time evolution, respectively Chevallier & Polarski (2001), Linder (2003). If we introduce the dimensionless Hubble parameter $E(z,\theta)$:

$$E(z,\theta) = \sqrt{(z+1)^2\Omega_k + (z+1)^3\Omega_m + \Omega_\Lambda e^{-\frac{3w_1 z}{z+1}}(z+1)^{3(w_0+w_1+1)}}, \tag{19}$$

we can define the luminosity distance and the modulus of distance. Actually the luminosity distance id given by:

$$d_L(z,\theta) = d_H(1 + z)d_M(z,\theta), \tag{20}$$

where $d_H = \frac{c}{H_0}$, $d_M(z,\theta)$ is the transverse comoving distance and it is defined as

$$d_M(z,\theta) = \begin{cases} \frac{d_H}{\sqrt{\Omega_k}}\sinh\frac{d_C(z,\theta)}{d_H} & \Omega_k > 0, \\ \frac{d_H}{\sqrt{|\Omega_k|}}\sin\frac{d_C(z,\theta)}{d_H} & \Omega_k < 0, \\ d_C(z,\theta) & \Omega_k = 0, \end{cases} \tag{21}$$

Table 1. Constraints on the cosmological parameters.

Calibrated GRB Hubble diagram and cosmology				
Id	$\langle x \rangle$	$\tilde{x}$	68% CL	95% CL
Ω_{m}	0.24	0.19	(0.12, 0.37)	(0.10, 0.58)
w_0	-0.29	-0.26	$(-0.5, -0.1)$	$(-1.01, 0.1)$
w_1	-0.12	-0.13	$(-0.43, 0.19)$	$(-0.88, 0.6)$
h	0.74	0.74	(0.69, 0.78)	(0.65, 0.8)
Ω_{m}	0.33	0.32	(0.19, 0.49)	(0.12, 0.59)
Ω_{Λ}	0.66	0.677	(0.51, 0.8)	(0.42, 0.87)
h	0.74	0.74	(0.70, 0.77)	(0.66, 0.79)
Ω_k	-0.00049	-0.00046	$(-0.007, 0.0064)$	$(-0.014, 0.013)$

Notes. Columns report the mean $\langle x \rangle$ and median $\tilde{x}$ values and the 68% and 95% confidence limits. The investigation of the CPL parametrization for the dark energy was performed assuming a flat universe (upper side). The analysis performed by assuming a non-zero spatial curvature is limited to the case $w = -1$ (non-flat ΛCDM). The GRB Hubble diagram alone provides $\Omega_{\mathrm{k}}^{\mathrm{median}} = -0.00046$, in agreement with the CMBR results.

being $d_{\mathrm{C}}(z, \theta)$ the comoving distance:

$$d_{\mathrm{C}}(z, \theta) = d_H \int_0^z \frac{\mathrm{d}\zeta}{E(\zeta, \theta)}, \tag{22}$$

therefore we can define the modulus of distance $\mu_{\mathrm{th}}(z, \theta)$:

$$\mu_{\mathrm{th}}(z, \theta) = 25 + 5 \log d_L(z, \theta) \cdot \tag{23}$$

The standard ΛCDM model corresponds to $w_0 = -1$, $w_1 = 0$.

To constrain the parameters specifying different cosmological models, we maximized the likelihood function $\mathcal{L}(\theta) \propto \exp\left[-\chi^2(\theta)/2\right]$, where θ indicates the set of cosmological parameters and the $\chi^2(\theta)$ was defined as usual by

$$\chi^2(\theta) = \sum_{i=1}^{N_{\mathrm{GRBs}}} \left[\frac{\mu_{\mathrm{obs}}(z_i) - \mu_{\mathrm{th}}(z_i, \theta)}{\sigma_i} \right]^2 . \tag{24}$$

Here, μ_{obs} and μ_{th} are the observed and theoretically predicted values of the distance modulus. The parameter space is efficiently sampled by using the MCMC method, thus running five parallel chains and using the Gelman-Rubin test to check the convergence Gelman & Rubin (1992). The confidence levels are estimated from the likelihood quantiles. We recall that we performed the analysis assuming a non-zero spatial curvature (not flat ΛCDM), and only in this case did we take $w = -1$. To alleviate the strong degeneracy of the curvature parameters and any EOS parameters, we added a Gaussian prior on Ω_k, centered on the value provided by the Planck Collaboration XVI (2014), $100\Omega_{\mathrm{k}}^{\mathrm{Planck}} = -4.2^{+4.3}_{-4.8}$, and with a dispersion ten times of $\sigma_{\Omega_{\mathrm{k}}}^{\mathrm{Planck}}$, where $100\sigma_{\Omega_{\mathrm{k}}}^{\mathrm{Planck}} = 4.5$. We investigated the CPL parameters assuming a flat universe. In a forthcoming paper we will present a full cosmological analysis using the high-redshift GRB Hubble diagram to test different cosmological models, where several parametrizations of the dark energy EOS will be used and also different dark energy scenarios, for instance the scalar field quintessence. In Table 1 we summarize the results of our analysis. There are indications that the dark energy EOS is evolving.

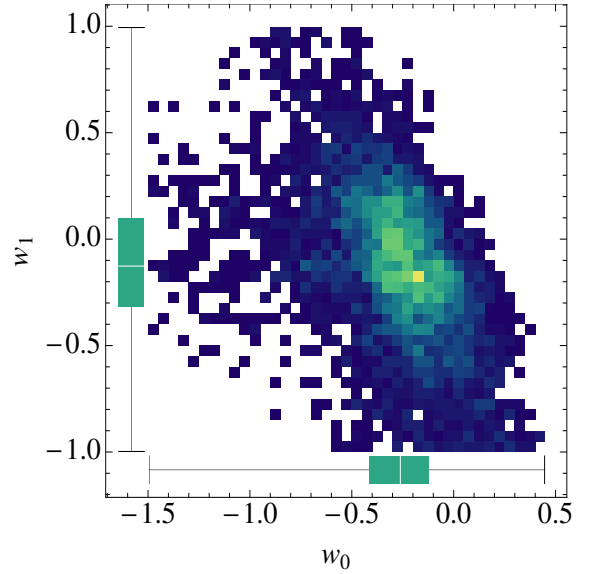The joint probability for different sets of parameters that characterize the CPL EOS is shown in Fig. 8.

Fig. 8. Regions of confidence for the marginalized likelihood function $\mathcal{L}(w_0, w_1)$. On the axes we also plot the box-and-whisker diagrams for the w_0 and w_1 parameters: the bottom and top of the diagrams are, as commonly done in the box-plots, the 25th and 75th percentile (the lower and upper quartiles, respectively), and the band near the middle of the box is the 50th percentile (the median). It is evident that the ΛCDM model, corresponding to $w_0 = -1$ and $w_1 = 0$ is not favored.

4. E_{iso} and $E_{\mathrm{p,i}}$ correlation

Since we here used the calibrated GRB Hubble diagram to perform the cosmological investigation described above, we discuss some arguments about the reliability of using the $E_{\mathrm{iso}} - E_{\mathrm{p,i}}$ relation for cosmological tasks. For instance, the calibration method we implemented so far relies on the underlying assumption that the calibration parameters do not evolve with redshift. It is worth noting that the problem of the redshift dependence of the GRBs correlations is widely debated in the literature, with different conclusions. This problem is intimately connected to the problem of the influence of possible selection effects or biases on the observed correlations, see, for instance, Li et al. (2008), Dainotti et al. (2013a,b), Liu & Wei (2015), Wang et al. (2016), Lin et al. (2016a,b). Any answer to these fundamental questions is far from being settled until more data with known redshifts are available. In this section, however, we revisit this question from an observational point of view: we test the validity of this commonly adopted working hypothesis and search for any evidence of such a redshift dependence. We also investigate possible effects on the GRB Hubble diagram. As a first simplified approach we considered two subsamples with a comparable number of bursts, divided according to redshift: a lower redshift sample of 97 bursts with $z \leq 2$, and a higher redshift sample of 67 burst with $z > 2$. We estimated the cosmological parameters for flat ΛCDM and CPL dark energy EOS cosmological models, considering the two subsamples separately, and compared the results. Even when the bursts belonging to these two samples experience different environment conditions, we did not find significant indication that a spurious z-evolution of the slope affects the cosmological fit: the values of the cosmological parameters derived from these two samples are statistically consistent within 1σ, as shown in Table 2. This result indirectly shows that redshift evolution dependence, even if it exists, does not undermine the reliability of the GRBs as probes of the cosmological

Table 2. Constraints on the cosmological parameters.

	Lower redshift sample				Higher redshift sample			
Id	$\langle x \rangle$	$\tilde{x}$	68% CL	95% CL	$\langle x \rangle$	$\tilde{x}$	68% CL	95% CL
				ΛCDM				
Ω_m	0.28	0.27	(0.15, 0.4)	(0.11, 0.48)	0.22	0.24	(0.14, 0.2)	(0.10, 0.35)
h	0.74	0.74	(0.70, 0.77)	(0.67, 0.8)	0.75	0.75	(0.72, 0.77)	(0.69, 0.8)
				CPL EOS				
Ω_m	0.21	0.18	(0.12, 0.33)	(0.10, 0.47)	0.19	0.20	(0.12, 0.27)	(0.11, 0.44)
h	0.74	0.74	(0.71, 0.77)	(0.66, 0.8)	0.74	0.74	(0.70, 0.77)	(0.67, 0.8)
w_0	−0.65	−0.61	(−0.77, −0.57)	(−0.83, −0.52)	−0.64	−0.63	(−0.75, −0.53)	(−0.86, −0.51)
w_1	−0.1	−0.11	(−0.3, 0.15)	(−0.47, 0.6)	−0.56	−0.57	(−0.63, −0.37)	(−0.69, 0.42)

Notes. Columns report the mean $\langle x \rangle$ and median $\tilde{x}$ values and the 68% and 95% confidence limits. The analysis is related to a spatially flat model with the dark energy parametrized through the CPL antsaz.

expansion. Moreover, to investigate this redshift dependence in more detail, that is, how it affects E_{iso} and/or $E_{p,i}$ (which we generically denote by y), we used two different approaches. First, we evaluated the Spearman rank correlation coefficient, $C(z, y)$, taking into account that since our sample is not too large, a few points could dominate the final value of the rank correlation, which would introduce a bias. We applied a *jacknife* resampling method by evaluating $C(z, y)$ for $N-1$ samples obtained by excluding one GRB at a time, and we adopted the mean value and the standard deviation to estimate $C(z, y)$. We found $C(z, E_{p,i}) = 0.299 \pm 0.004$, and $C(z, E_{iso}) = 0.278 \pm 0.004$, which indicates a moderate evolution of the correlation. The Spearman rank correlation coefficient, however, does not include the errors of E_{iso} and $E_{p,i}$, so that we also implemented an alternative, and completely different, approach to determine whether and how strongly these variables are correlated with redshift. We assumed that the evolutionary functions can be parametrized by a simple power-law functions: $g_{iso}(z) = (1+z)^{k_{iso}}$ and $g_p(z) = (1+z)^{k_p}$ (see for instance Dainotti et al. 2013a), so that $E'_{iso} = E_{iso}/g_{iso}(z)$ and $E'_{p,i} = E_{p,i}/g_p(z)$ are the de-evolved quantities. In this case, the effective $E_{iso} - E_{p,i}$ correlation can be written as a 3D correlation:

$$\log\left[\frac{E_{iso}}{1\ \text{erg}}\right] = b + a \log\left[\frac{E_{p,i}}{300\ \text{keV}}\right] + \left(k_{iso} - a\,k_p\right) \log\left(1+z\right).$$
(25)

Calibrating this 3D relation means determining the coefficients $(a, b, k_{iso}, \text{and } k_p)$ plus the intrinsic scatter σ_{int}. Low values for k_{iso} and k_p would indicate a lack of evolution, or at least negligible evolutionary effects. To fit these coefficients, we constructed a 3D Reichart likelihood, but we consider no error on the redshift of each GRB:

$$L_{\text{Reichart}}^{3D}(a, k_{iso}, k_p, b, \sigma_{int}) = \frac{1}{2} \frac{\sum \log\left(\sigma_{int}^2 + \sigma_{y_i}^2 + a^2\sigma_{x_i}^2\right)}{\log\left(1+a^2\right)}$$
$$+ \frac{1}{2} \sum \frac{(y_i - ax_i - (k_{iso} - \alpha)z_i - b)^2}{\sigma_{int}^2 + \sigma_{x_i}^2 + a^2\sigma_{x_i}^2},$$
(26)

where $\alpha = a\,k_p$. As in the 2D case, we maximized our likelihood in the space $(a, k_{iso}, \text{and } \alpha)$ since b was evaluated analytically by

solving the equation $\frac{\partial}{\partial b} L_{\text{Reichart}}^{3D}(a, k_{iso}, k_p, b, \sigma_{int}) = 0$, we obtain

$$b = \left[\sum \frac{y_i - ax_i - (k_{iso} - \alpha)z_i}{\sigma_{int}^2 + \sigma_{y_i}^2 + a^2\sigma_{x_i}^2}\right]\left[\sum \frac{1}{\sigma_{int}^2 + \sigma_{y_i}^2 + a^2\sigma_{x_i}^2}\right]^{-1}.$$
(27)

We also used the MCMC method and ran five parallel chains and the Gelman-Rubin convergence test, as previously explained. We finally studied the median and 68% confidence range of k_{iso} and α to test whether the correlation evolves and noted that a null value for these parameters is strong evidence for a lack of any evolution. We found that $a = 1.86^{+0.07}_{-0.09}$, $k_{iso} = -0.04 \pm 0.1$; $\alpha = -0.02 \pm 0.2$; $\sigma_{int} = 0.35 \pm 0.03$, so that $b = 52.40^{+0.03}_{-0.06}$. We can safely conclude that the E_{iso} and $E_{p,i}$ correlation shows, at this stage, weak indications of evolution. In Fig. 9 we plot both the de-evolved and evolved/original correlation, and the de-evolved and evolved/original Hubble diagram: we do not see any signs of evolution.

5. Fully Bayesian analysis

In this section we simultaneously constrain the calibration parameters (a, b, σ_{int}) and the set of cosmological parameters by considering the same likelihood function as in Eq. (7). Our task is to determine the multidimensional probability distribution function (PDF) of the parameters $\{a, b, \sigma_{int}, \boldsymbol{p}\}$, where $\boldsymbol{p}$ is the $\mathcal{N}$-dimensional vector of the cosmological parameters. The Amati correlation can be written in the form

$$\log_{10} S_{bol} = a + b \log_{10} E_{p,i} - \log_{10}[4\pi d_L^2(z, \boldsymbol{p})].$$
(28)

We note that the best-fit zero point b can be analytically expressed as a function of (a, σ_{int}) when the cosmological parameter $\boldsymbol{p}_c$ is specified. A more computationally efficient strategy is to let b free and add it to the list of quantities to be determined, which thus sums up to $\mathcal{N} + 3$. To efficiently sample the $\mathcal{N} + 3$ dimensional parameter space, we used the MCMC method and ran five parallel chains and used the Gelman-Rubin convergence test, as described in the previous section. Since we are mainly interested in the calibration problem and not in constraining the cosmological parameters $(\Omega_M, \Omega_\Lambda, h)$, we considered here only the particular case of a flat ΛCDM model, as already done in the

Table 3. Constraints on the calibration parameters.

Id	\langle x\rangle	$\tilde{x}$	68% CL	95% CL	$\langle x\rangle$	$\tilde{x}$	68% CL	95% CL
		Fully Bayesian analysis				Local regression with SNIa		
a	1.69	1.71	(1.64, 1.76)	(1.59, 1.82)	1.74	1.74	(1.59, 1.93)	(1.45, 2.16)
b	52.5	52.5	(52.48, 52.55)	(52.44, 52.60)	–	–	–	–
σ_{int}	0.23	0.23	(0.22, 0.25)	(0.20, 0.26)	0.36	0.37	(0.33, 0.49)	(0.31, 0.5)

Notes. Columns report the mean $\langle x\rangle$ and median $\tilde{x}$ values and the 68% and 95% confidence limits. The calibration procedure based on the local regression technique does not directly provide the zero-point parameter b, which can be analytically evaluated as a function of (a, σ_{int}) by Eq. (27). The fully Bayesian analysis, furthermore, is related to a spatially flat model with dark energy parametrized through the CPL antsaz.
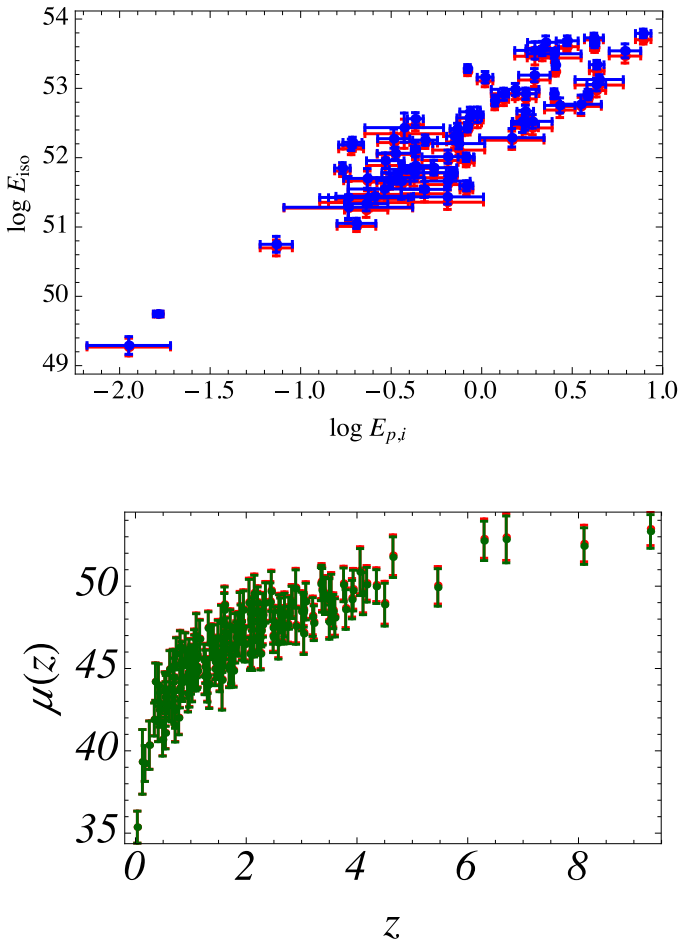

Fig. 9. Evolutionary effects on the $E_{iso} - E_{p,i}$ correlation and the Hubble flow. *Upper panel*: de-evolved (red points) and evolved/original correlation (green poins); there is no discernable evolution. *Bottom panel*: de-evolved (red points) and evolved/original (green points) Hubble diagram; evolutionary effects of the correlation do not affect the GRB Hubble diagram.

Fig. 10. Regions of confidence for the marginalized likelihood function $\mathcal{L}(a, \sigma)$, obtained by marginalizing over b and the cosmological parameters. The gray regions indicate the 1σ (full zone) and 2σ (empty zone) regions of confidence. On the axes we also plot the box-and-whisker diagrams for the a and σ_{int} parameters: the bottom and top of the diagrams are the 25th and 75th percentile (the lower and upper quartiles, respectively), and the band near the middle of the box is the 50th percentile (the median).

previous analysis. The analysis determines, at the same time, the cosmological parameters and the correlation coefficients, which are listed in Table 3. Although the calibration procedure is different (since we now fit for the cosmological parameters as well), it is nevertheless worth comparing this determination of (a, b, σ_{int}) with the one obtained in the previous analysis based on the SNIa sample. It is evident that although the median values change, the 95% confidence levels are in full agreement so that we cannot
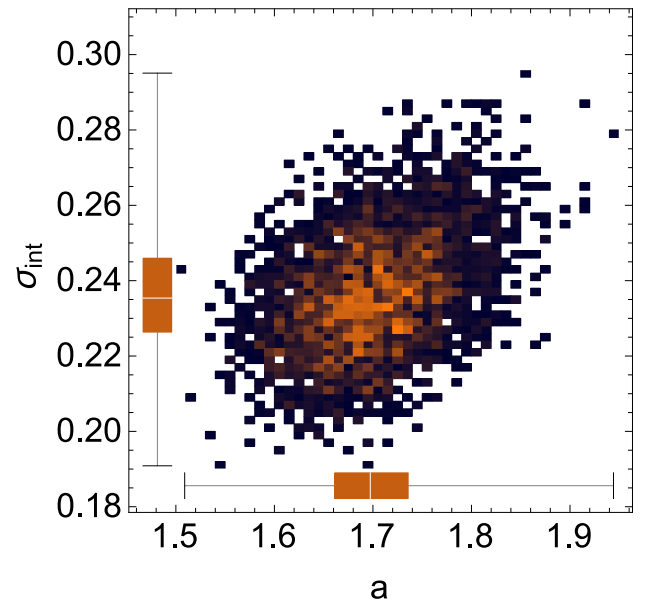
find any statistically significant difference. Figure 10 shows the marginalized probability distribution function of the correlation coefficients of the relation $E_{iso} - E_{p,i}$.

As far as the cosmological parameters are concerned, it turns out that $\Omega_m^{median} = 0.25$, the range of confidence at 1σ is (0.13, 0.54), and $\Omega_\Lambda^{median} = 0.75$, the range of confidence at 1σ is (0.50, 0.87). This result implies that $\Omega_k^{median} = -0.0006$, and that the range of confidence is $(-0.00730, 0.00605)$, in a good agreement with results derived by using the calibrated GRBs Hubble diagram.

Also in this case we finally estimate the distance modulus for each ith GRB in our sample at redshift z_i, to build the fiducial Hubble diagram, by using Eqs. (1) and (10). It turns out that the fiducial and calibrated Hubble diagrams are fully statistically consistent, as shown in Fig. 11.
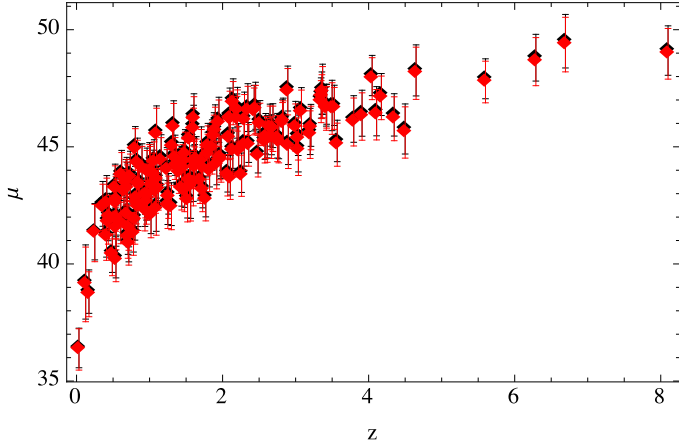
Fig. 11. Fiducial GRB Hubble diagram, superimposed on the calibrated Hubble diagram.

6. Discussion and conclusions

The $E_{p,i}-E_{iso}$ correlation is one of the most intriguing properties of the long GRBs, with significant implications for the use of GRBs as cosmological probes. Here we explored the Amati relation in a way independent of the cosmological model. Using the recently updated data set of 162 high-redshift GRBs, we applied a local regression technique to estimate the distance modulus using the recent Union SNIa sample (Union2.1). The derived calibration parameters are statistically fully consistent with the results of our previous work Demianski et al. (2011). Moreover, we tested the validity of the commonly adopted working hypothesis that the GRB Hubble diagram is slightly affected by redshift dependence of the $E_{p,i}-E_{iso}$ correlation. As a first qualitative and simplified approach we considered a *lower redshift sample* of 97 bursts with $z \leq 2$, and a higher redshift sample of 67 burst with $z > 2$. We estimated the cosmological parameters for flat ΛCDM and CPL dark energy EOS cosmological models, considering the two subsamples separately, and compared the results. Even when the bursts belonging to these two samples had different environment conditions, we found no significant indications that a spurious z-evolution of the slope affected the cosmological fit. Moreover, to quantify this redshift dependence, we used two different approaches. First, we evaluated the Spearman rank correlation coefficient, $C(z, y)$ by applying a jacknife resampling method by evaluating $C(z, y)$ for $N-1$ samples obtained by excluding one GRB at a time, and we adopted the mean value and the standard deviation to estimate $C(z, y)$. $C(z, E_{p,i}) = 0.299 \pm 0.004$, and $C(z, E_{iso}) = 0.278 \pm 0.004$, which indicates a negligible evolution of the correlation. Moreover, we also implemented an alternative method, assuming that the redshift evolution can be parametrized by simple power-law functions: $g_{iso}(z) = (1 + z)^{k_{iso}}$ and $g_p(z) = (1 + z)^{k_p}$ and that the correlation holds for the de-evolved quantities $E'_{iso} = E_{iso}/g_{iso}(z)$ and $E'_{p,i} = E_{p,i}/g_p(z)$. In this case, we rewrote an effective 3D $E_{iso} - E_{p,i}$ correlation, with included the evolutionary terms. Since we were interested in the implications of possible evolutionary effects of the GRB Hubble diagram and to simplify the fit, we introduced an auxiliary variable $\alpha = ak_p$. A null value for k_{iso} and α is strong evidence for a lack of any evolution. To fit the coefficient of our 3D correlation we constructed a 3D Reichart likelihood and used a MCMC method running five parallel chains and using the Gelman-Rubin convergence test. The E_{iso}

and $E_{p,i}$ correlation shows at this stage only weak indications of evolution. The derived calibration parameters were used to construct an updated calibrated GRB Hubble diagram, which we adopted as a tool to constrain the cosmological models and to investigate the dark energy EOS. In particular, we searched for any indications that $w(z) \neq -1$, which reflects the possibility of a deviation from the ΛCDM cosmological model. To accomplish this task, we focused on the CPL parametrization as an example. To efficiently sample the cosmological parameter space, we again used a MCMC method. At 1σ level we found indications for a time evolution of the EOS in the considered parametrization; we conclude that the ΛCDM model is not favored even though it is not ruled out by these observations so far. Moreover, for $w = -1$ we also performed our analysis assuming a non-zero spatial curvature, adding a Gaussian prior on Ω_k centered on the value provided by the *Planck* data Planck Collaboration XVI (2014). The GRB Hubble diagram alone provides $\Omega_k^{median} = -0.00046$ for the range of confidence at 1σ ($-0.007, 0.0064$). Finally, to investigate the reliability of the $E_{p,i}-E_{iso}$ correlation in greater detail, we also used a different method to simultaneously extract the correlation coefficients and the cosmological parameters of the model from the observed quantities. To illustrate this method we assumed here, by way of an example, only the particular case of a non-flat ΛCDM model, as already done in the previous analysis. This analysis simultaneously determines the cosmological parameters and the correlation coefficients. Although the calibration procedure is different (since we now fit for the cosmological parameters as well), it is nevertheless worth comparing this determination of (a, b, σ_{int}) with the one obtained in the previous analysis based on the SNIa sample. It is evident that although the median values change, the 95% confidence levels are in full agreement so that we cannot find any statistically significant difference. This means that the high-redshift GRBs can be used as cosmological probes, mainly in a redshift region, $z \gtrsim 3$, which is unexplored by SNIa and BAO samples, and that both the calibration technique based on a local regression with SNIa and a fully Bayesian approach are reliable. As a final remark we note that our results for the cosmological parameters are statistically consistent with those previously obtained by other teams, as shown in Table 6, where we display some of the most recent measurements of cosmological parameters obtained with GRBs, even if following a slightly different approach. The main peculiarity in our analysis consists of the procedure used to build up the dataset, consisting of 162 objects, as discussed in Sect. 2.1 (see also Sawant & Amati, in prep.), even more than the specific statistical analysis, which follows a Bayesian approach through the implementation of the MCMC. Because the reliability of GRBs as distance indicators has not yet been clearly proved and because it constitutes an independent topic in the field of GRB research, it is not meaningless to investigate the reliability of the $E_{p,i}-E_{iso}$ correlation whenever new and improved datasets are available. In the near future we intend to enhance the cosmological analysis by using the high-redshift GRB Hubble diagram to test different cosmological models, where several parametrizations of the dark energy EOS are used, but a cosmographic approach will also be implemented, which will update the analysis performed in Demianski et al. (2012) to check whether with this new updated dataset the estimates of the jerk and the dark energy parameters will confirm deviations from ΛCDM cosmological model, as has been indicated in our previous analysis.

Table 4. Derived distance moduli for the low redshift subsample, consisting of the GRBs whose redshifts cross the range spanned by the SNIa.

	Calibrated GRBs Hubble diagram: the *low redshift* subsample						
GRBs ID	Redshift	μ	σ_μ	$E_{p,i}$ (keV)	$\sigma_{E_{p,i}}$	E_{iso} (10^{52} erg)	$\sigma_{E_{iso}}$
060 218	0.03351	35.1195	0.933638	4.9	0.3	0.00535399	0.000259064
060 614	0.125	38.6856	1.84671	55.	45.	0.216774	0.0867097
030 329	0.17	38.4667	1.03564	100.	23.	1.47701	0.260648
020 903	0.25	39.9357	1.38443	3.37	1.79	0.00244119	0.000610299
130 427A	0.3399	40.6749	0.95616	1250.	150.	77.0134	7.87637
011 121	0.36	42.9717	1.07033	1060.	275.	7.97042	2.18968
020 819B	0.41	40.8059	1.1032	70.	21.	0.693324	0.175525
101 213A	0.414	42.8313	1.21619	440.	180.	2.72107	0.526658
990 712	0.434	41.5047	0.985045	93.	15.	0.685192	0.131768
010 921	0.45	41.8452	1.0036	129.	26.	0.966894	0.0966894
091 127	0.49	39.7308	0.946699	51.	5.	1.64622	0.176066
081 007	0.5295	42.6995	1.03825	61.	15.	0.176323	0.0176323
090 618	0.54	39.9036	0.925708	250.404	4.466	28.5912	0.523898
100 621A	0.542	41.4047	0.975989	146.	23.	2.82246	0.352807
060 729	0.543	42.2564	1.32376	77.	38.	0.423384	0.0882049
090 424	0.544	42.0376	0.927353	249.974	3.3196	4.06569	0.352833
101 219B	0.55	42.5063	0.951189	108.	12.	0.626413	0.061759
050 525A	0.606	41.6888	0.940851	129.	6.5	2.29843	0.486207
110 106B	0.618	43.7538	1.07668	194.	56.	0.734033	0.0707502
050 416A	0.6528	41.8718	1.00894	22.	4.5	0.10625	0.0177083
111 209A	0.677	43.7533	0.983363	520.	89.	5.13951	0.620285
080 916A	0.689	43.868	0.93225	208.	11.	0.975114	0.0886467
020 405	0.69	42.2854	0.928094	354.	10.	10.6379	0.886495
970 228	0.695	43.1984	1.11582	195.	64.	1.64915	0.124129
991 208	0.706	41.2777	0.945272	313.	31.	22.972	1.8626
111 228A	0.716	40.4242	0.95484	58.	7.	2.75042	0.26617
041 006	0.716	41.2868	1.01881	98.	20.	3.10531	0.887233
090 328	0.736	44.393	0.9305	1157.91	55.552	14.1806	0.997201
030 528	0.78	40.8528	0.974974	57.	9.	2.22246	0.266695
051 022	0.8	42.3122	1.13123	754.	258.	56.0394	5.33709
100 816A	0.8049	44.9536	0.94066	247.	20.	0.711714	0.0889643
110 715A	0.82	42.816	0.942884	220.	20.	4.36118	0.445018
970 508	0.835	44.1715	1.08963	145.	43.	0.632199	0.133563
990 705	0.842	42.7009	1.09192	459.	139.	18.7026	2.6718
000 210	0.846	43.8624	0.92956	753.	26.	15.4091	1.69233
040 924	0.859	43.1051	1.13207	102.	35.	0.980131	0.0891028
091 003	0.8969	44.5543	0.999868	810.	157.	10.7036	1.78393
080 319B	0.937	42.9071	0.931116	1261.	65.	117.866	8.92921
071 010B	0.947	42.1526	1.03421	88.	21.	2.3222	0.40192
970 828	0.958	42.9866	1.00157	586.	117.	30.3759	3.57364
980 703	0.966	44.2503	0.957411	503.	64.	7.41683	0.714875
091 018	0.971	42.7535	1.19374	55.	20.	0.625596	0.348546
980 326	1.	43.5588	1.33824	71.	36.	0.500843	0.0983799
021 211	1.01	43.7735	1.20912	127.	52.	1.16296	0.134188
991 216	1.02	42.444	1.00615	648.	134.	69.7948	7.15844
080 411	1.03	43.6536	0.95959	524.	70.	16.1999	0.984526
000 911	1.06	44.5421	1.00544	1856.	371.	69.8621	14.3307
091 208B	1.063	44.5447	0.945957	246.	25.	2.06018	0.179146
110 213B	1.083	43.1534	0.974899	256.	40.	8.3342	1.34423
091 024	1.092	43.1454	0.93459	396.225	25.3132	18.3765	1.99258
980 613	1.096	45.4997	1.27239	194.	89.	0.609565	0.0986062
080 413B	1.1	44.1225	1.08084	163.	47.5	1.6137	0.268951
981 226	1.11	43.7092	1.27607	87.	40.	0.807035	0.179341
000 418	1.12	43.2984	0.940538	284.	21.	9.50723	1.79382
061 126	1.1588	45.0298	1.09402	1337.	410.	31.4187	3.59071
090 926B	1.24	43.924	0.945337	212.	21.	4.13637	0.449605
020 813	1.25	42.8407	1.05146	590.	151.	68.3538	17.0885
061 007	1.262	43.3478	0.963166	890.	124.	89.9608	8.99608
130 420A	1.297	42.4236	0.945544	129.	13.	7.74195	0.720181
990 506	1.3	42.8153	1.02406	677.	156.	98.1304	9.90306
061 121	1.314	45.6168	0.953501	1289.	153.	23.5036	2.70156
071 117	1.331	42.5292	1.34174	112.	56.	5.85526	2.70243
070 521	1.35	44.8194	0.949447	522.	55.	10.8135	1.80226
100 414A	1.368	44.812	0.942611	1295.	120.	54.987	5.40856
120 711A	1.405	44.7159	0.94466	2340.	230.	180.405	18.0405
100 814A	1.44	43.2858	0.95932	259.	34.	15.3438	1.80515
050 318	1.4436	43.8132	1.01313	115.	25.	2.30171	0.162473
110 213A	1.46	44.1083	1.11878	224.	74.	5.77844	0.812593

Notes. Column (1) lists the GRBs ID. Column (2) lists the redshift. Column (3) lists the estimated distance modulus $\mu(z)$. Column (4) lists the error σ_μ. Column (5) lists $E_{p,i}$. Column (6) lists $\sigma_{E_{p,i}}$. Column (7) lists E_{iso}. Column (8) lists $\sigma_{E_{iso}}$.

Table 5. Derived distance moduli for the high redshift subsample, consisting of the GRBs whose redshifts pass through the range spanned by the SNIa.

Calibrated GRBs Hubble diagram: the high redshift subsample							
GRBs ID	Redshift	μ	σ_μ	$E_{p,i}$ (keV)	$\sigma_{E_{p,i}}$	E_{iso} (10^{52} erg)	$\sigma_{E_{iso}}$
120 724A	1.48	43.9951	1.0662	69.	19.	0.848992	0.180637
10 222	1.48	43.5582	0.929143	766.	30.	84.8992	9.03183
60 418	1.489	45.0134	1.043	572.	143.	13.5498	2.70995
30 328	1.52	42.871	0.978916	328.	55.	38.8622	3.61509
90 102	1.547	45.9243	0.946461	1174.	120.	22.604	2.71248
70 125	1.547	44.0644	0.973486	934.	148.	84.087	8.4087
40 912	1.563	42.781	1.69995	44.	33.	1.35658	0.361755
100 728A	1.567	43.8473	0.927328	833.	23.	86.8265	8.13998
990 123	1.6	44.1755	1.0596	1724.	466.	240.703	38.9106
71 003	1.604	46.5316	0.962389	2077.	286.	38.2795	4.52476
090 418A	1.608	46.8731	1.03718	1567.	384.	17.1951	2.71502
110 503A	1.613	44.6927	0.948442	551.	60.	20.8167	1.81015
990 510	1.619	44.3532	0.946002	423.	42.	18.1031	2.71546
80 605	1.64	45.0375	0.958753	766.	55.	28.0685	14.4869
80 928	1.6919	43.2837	1.03666	95.	23.	3.98686	0.906105
91 020	1.71	45.675	0.960875	507.228	68.208	8.4289	1.0876
10 0906A	1.727	43.2599	0.973643	289.	46.	29.916	2.71963
12 0119A	1.728	44.3889	0.946023	496.	50.	27.1967	3.62623
110 422A	1.77	42.9739	0.944986	421.	42.	79.8218	8.1636
12 0326A	1.798	44.5549	0.94189	152.	14.	3.26663	0.272219
08 0514B	1.8	45.3824	0.948821	627.	65.	18.1484	3.62968
09 0902B	1.822	44.7661	0.925467	2187.	31.	292.271	9.07675
110 801A	1.858	45.1695	1.23345	400.	171.	10.897	2.72425
60 908	1.8836	46.2739	1.28842	553.	260.	7.1761	1.90757
20 127	1.9	45.7854	1.13272	290.	100.	3.72504	0.109025
60 814	1.9229	44.6651	1.11463	751.	246.	56.7086	5.27099
80 3190	1.95	46.5089	1.08858	906.	272.	14.9089	2.99996
81 008	1.9685	44.6084	0.999689	261.	52.	10.002	0.909269
30 226	1.98	44.5553	1.02204	289.	66.	12.7314	1.36408
081 203A	2.05	46.8257	1.31834	1541.	756.	31.853	11.8311
926	2.07	43.9293	0.936188	310.	20.	28.5827	6.18989
80 207	2.0858	44.6893	1.56663	333.	222.	16.3877	1.82086
061 222A	2.088	45.8633	0.983381	874.	150.	30.0449	6.37315
100 728B	2.106	46.3176	0.965919	323.	47.	3.55142	0.364248
90 926	2.1062	43.7433	0.925125	900.798	7.02001	228.014	2.27338
11 211	2.14	44.7932	0.957566	186.	24.	5.73888	0.637653
71 020	2.145	47.4073	0.984835	1013.	160.	10.0208	4.5549
509 220	2.199	46.4216	1.06071	415.	111.	5.55991	1.82292
121 128A	2.2	44.9272	0.931098	243.	13.	8.65897	0.820323
80 804	2.2045	46.8579	0.931104	810.	45.	12.0319	0.546906
110 205A	2.22	45.2389	1.20041	757.	305.	48.3171	6.38151
81 221	2.26	43.8782	0.929903	284.	14.	31.9195	1.82397
130 505A	2.27	45.029	0.935913	2030.	150.	346.586	27.3621
60 124	2.296	45.502	1.15448	784.	285.	43.7896	6.38599
21 004	2.3	46.2112	1.2461	266.	117.	3.46681	0.456159
051 109A	2.346	46.8641	1.16259	539.	200.	6.84516	0.730151
080 413A	2.433	46.867	1.09682	584.	180.	8.58559	2.10073
90 812	2.452	47.364	1.13965	2000.	700.	47.5021	8.22152
120 716A	2.486	44.8287	0.944518	397.	40.	30.1538	0.274125
130 518A	2.488	45.181	0.942494	1382.	130.	192.805	18.2753
81 121	2.512	45.5879	0.934876	608.	42.	32.3534	3.65576
81 118	2.58	44.4939	0.943808	203.308	20.	13.9705	0.888677
80 721	2.591	46.1254	0.958853	1741.	227.	133.515	22.8622
50 820	2.615	45.9102	1.00661	1325.	277.	103.356	8.23186
30 429	2.65	45.6525	1.00258	128.	26.	2.28721	0.274465
120 811C	2.671	45.3823	0.943181	198.	19.	6.40514	0.640514
080 603B	2.69	46.1013	1.16024	277.	100.	6.03994	3.05658
91 029	2.752	45.5087	1.07352	230.	66.	7.96513	0.823979
81 222	2.77	46.0964	0.9302	630.344	31.2156	27.3822	2.74693
50 603	2.821	46.6406	0.937652	1333.	107.	64.1164	4.57975

Notes. Column (1) lists the GRBs ID. Column (2) lists the redshift. Column (3) lists the estimated distance modulus $\mu(z)$. Column (4) lists the error σ_μ. Column (5) lists $E_{p,i}$ (keV). Column (6) lists $\sigma_{E_{p,i}}$. Column (7) lists E_{iso}. Column (8) lists $\sigma_{E_{iso}}$.

Table 5. continued.

GRBs ID	Redshift	μ	σ_μ	$E_{p,i}$ (keV)	$\sigma_{E_{p,i}}$	E_{iso} (10^{52} erg)	$\sigma_{E_{iso}}$
			Calibrated GRBs Hubble diagram: the high redshift subsample				
110 731A	2.83	46.6737	0.930181	1164.	58.	49.4641	4.58001
111 107A	2.893	47.598	1.08191	420.	124.	3.7571	0.54982
50 401	2.8983	45.3038	1.02857	467.	110.	37.5723	7.33118
090 715B	3.	46.1498	1.10789	536.	172.	23.8409	3.66783
80 607	3.036	46.0503	0.959184	1691.	226.	199.938	11.0058
81 028	3.038	44.8963	1.19331	234.	93.	18.3432	1.83432
060 607A	3.075	46.7497	1.03846	478.	118.	11.9256	2.75205
20 124	3.2	45.7872	1.11734	448.	148.	28.4571	2.75391
60 526	3.22	45.5887	1.00027	105.	21.	2.7542	0.367227
80 810	3.35	47.5973	0.954116	1470.	180.	47.7705	5.51198
110818A	3.36	47.7168	1.01118	1116.	240.	26.6425	2.75612
30 323	3.37	47.4274	1.22111	270.	113.	2.94001	0.918752
971 214	3.42	47.0429	0.996013	685.	133.	22.0553	2.75691
60 707	3.424	47.0792	1.05247	274.	72.	4.31924	1.10278
60 306	3.5	46.7831	1.23155	315.	135.	7.63024	1.01124
980 329	3.5	45.2884	0.974999	1096.	176.	266.599	53.3198
60 115	3.5328	46.978	1.1415	297.	102.	5.88442	3.7697
90 323	3.57	45.8457	0.986639	1901.	343.	437.725	53.3362
130 514A	3.6	45.6286	1.09246	497.	152.	52.4234	9.19708
130 408A	3.758	47.5053	0.963238	1000.	140.	34.9716	6.44214
120 802A	3.796	46.1613	1.12782	274.	93.	12.8862	2.76133
60 210	3.91	46.6447	1.11229	574.	187.	32.2294	1.84168
120 909A	3.93	47.0881	1.17098	1276.	483.	87.4863	10.13
60 206	4.0559	48.3284	1.27013	410.	187.	4.14595	1.93478
90 516	4.109	46.899	1.19876	971.	390.	71.8762	13.8223
120 712A	4.1745	47.4784	1.00188	641.	130.	21.1989	1.84338
080 916C	4.35	47.145	0.960048	2760.	369.	406.692	85.765
131	4.5	46.1465	1.22279	987.	416.	183.6	32.2915
90 205	4.6497	49.1939	1.1254	214.	72.	0.8307	0.2769
60 927	5.46	47.1793	1.06039	275.	75.	12.0218	2.77427
50 904	6.295	49.5673	1.13213	3178.	1094.	133.364	13.8921
80 913	6.695	49.788	1.31553	710.	350.	9.1742	2.68739
90 423	8.1	49.2684	1.0345	410.	100.	8.81815	2.0653
090 429B	9.3	50.0158	0.959439	433.	58.	6.69027	1.30089

Table 6. Some of the most recent constraints of cosmological parameters by GRBs.

Data	Cosmological model	Constraint	Reference
GRB	flat ΛCDM	$\Omega_m = 0.23^{+0.06}_{-0.04}$	Wang et al. (2016)
GRB	flat ΛCDM	$\Omega_m = 0.302 \pm 0.142$	Lin et al. (2016a)
GRB+SNeIa+Bao+Planck	flat ΛCDM	$\Omega_m = 0.2903^{+0.0109}_{-0.0106}$	Liu & Wei (2015)
GRB	flat ΛCDM	$\Omega_m = 0.29^{+0.23}_{-0.15}$	Izzo et al. (2015)

References

Alam, U., Sahni, V., Saini, T. D., & Starobinsky, A. A. 2003, MNRAS, 344, 1057
Amati, L. 2006, MNRAS, 372, 233
Amati, L., Frontera, F., Tavani, M., et al. 2002, A&A, 390, 81
Amati, L., Della Valle, D., Frontera, F., et al. 2007, A&A, 463, 913
Amati, L., Guidorzi, C., Frontera, F., et al. 2008, MNRAS, 391, 577
Amati, L., Frontera, F., & Guidorzi, C. 2009, A&A, 508, 173
Amati, L., & Della Valle, M. 2013, Int. J. Mod. Phys. D, 22, 30028
Amanullah, R., Lidman, C., Rubin, D., et al. 2010, ApJ, 71, 712
Antonelli, A. L., D'Avanzo, P., Perna, R., et al. 2009, A&A, 507, L45
Astier, P., Guy, J., Regnault, N., et al. 2006, A&A, 447, 31
Band, D. L., & Preece, R. D. 2005, ApJ, 627, 319
Band, D., Matteson, J., Ford, L., et al. 1993, ApJ, 413, 281
Basak, R., & Rao, A. R. 2013, MNRAS, 436, 3082
Butler, N. R., Kocevski, D., Bloom, J. S., et al. 2007, ApJ, 671, 656
Cabrera, J. I., Firmani, C., Avila-Reese, V., et al. 2007, MNRAS, 382, 342
Cardone, V. F., Capozziello, S., & Dainotti, M. G. 2008, MNRAS, 391, L79
Carroll, S. M. 2001, Liv. Rev. Relativ., 4, 1
Chevallier, M., & Polarski, D. 2001, Int. J. Mod. Phys. D, 10, 213
Clarkson, C., & Maartens, R. 2010, Class. Quant. Gravity, 27, 124008
Cucchiara, A., Levan, A. J., Fox, D. B., et al. 2011, ApJ, 736, 7
D'Agostini, G. 2005, [arXiv:physics/0511182]
Dai, Z. G., Liang, E. W., & Xu, D. 2004, ApJ, 612, L101
Dainotti, M. G., Petrosian, V., Singal, J., & Ostrowski, M. 2013a, ApJ, 774, 157
Dainotti, M. G., Cardone, V. F., Piedipalumbo, E., & Capozziello, S. 2013b, MNRAS, 436, 82
Diaferio, A., Ostorero, L., & Cardone, V. F. 2011, JCAP, 10, 008
Dichiara, S., & Amati, L. 2013, Acta Politechnica, 53, 687
Demianski, M., Piedipalumbo, E., & Rubano, C. 2011, MNRAS, 411, 1213
Demianski, M., Piedipalumbo, E., Rubano, C., & Scudellaro, P. 2012, MNRAS, 426, 13961415
Friedman, A. S., & Bloom, J. S. 2005, ApJ, 627, 1
Frontera, F., Amati, L., Guidorzi, C., Landi, R., & in't Zand, J. 2012, ApJ, 754, 138
Gao, H., Liang, N., & Zhu, Z.-H. 2012, Int. J. Mod. Phys. D, 21, 1250016-1

Gelman, A., & Rubin, D. B. 1992, Stat. Sci., 7, 457
Ghirlanda, G., Ghisellini, G., & Lazzati, D. 2004, ApJ, 616, 331
Ghirlanda, G., Ghisellini, G., Firmani, C., Celotti, A., & Bosnjak, Z. 2005, MNRAS, 360, L45
Ghirlanda G., Ghisellini G., & Firmani C. 2006, New J. Phys., 8, 123
Ghirlanda, G., Nava, L., Ghisellini, G., Firmani, C., & Cabrera, J. I. 2008, MNRAS, 387, 319
Ghirlanda, G., Nava, L., & Ghisellini, G. 2010, A&A, 511, A43
Golenetskii, S. V., Mazets, E. P., Aptekar, R. L., & Ilinskii, V. N. 1983, Nature, 306, 451
Kodama, Y., Yonetoku, D., Murakami, T., et al. 2008, MNRAS, 391, L1
Lamb, D. Q., Donaghy, T. Q., & Graziani, C. 2005, ApJ, 620, 355
Izzo, L., Muccino, M., Zaninoni, E., Amati, L., & Della Valle, M. 2015, A&A, 582, A115
Liang, N., Xiao, W. K., Liu, Y., & Zhang, S. N. 2008, ApJ, 685, 354
Lin, H.-N., Li, X., Liu, Y., Wang, S., & Chang, Z. 2015, MNRAS, 453, 128
Lin, H.-N., Li, X., & Chang, Z. 2016a, MNRAS, 455, 2131
Lin, H.-N., Li, X., & Chang, Z. 2016b, MNRAS, 459, 2501
Liu, J., & Wei, H. 2015, General Relativity and Gravitation, 47, 141
Linder, E. V. 2003, Phys. Rev. Lett., 90, 091301
Meszaros, P. 2006, Rep. Prog. Phys., 69, 2259
Nakar, E., & Piran, T. 2005, MNRAS, 360, L36
Nava, L., Salvaterra, R., Ghirlanda, G., et al. 2012, MNRAS, 421, 1256
Perlmutter, S., Aldering, G., della Valle, M., et al. 1998, Nature, 391, 51
Perlmutter, S., Aldering, G., Goldhaber, G., et al. 1999, ApJ, 517, 565
Planck Collaboration XVI. 2014, A&A, 571, A16
Planck Collaboration XIII. 2016, A&A, 594, A13
Postnikov, V. S., Dainotti, M. G., Hernandez, X., & Capozziello, S. 2014, ApJ, 783, 126
Reichart, D. E., Lamb, D. Q., Fenimore, E. E., et al. 2001, ApJ, 552, 57
Riess, A. G., Filippenko, A. V., Challis, P., et al. 1998, AJ, 116, 1009
Riess, A. G., Strolger, L.-G., Tonry, J., et al. 2004, ApJ, 607, 665
Riess, A. G., Strolger, L. G., Casertano, S., et al. 2007, ApJ, 659, 98
Sahni, V., Saini, T. D., Starobinsky, A. A., & Alam, U. 2003, JETP Lett., 77, 201
Sakamoto, T., Hullinger, D., Sato, G., Yamazaki, R., & Barbier, L. 2008a, ApJ, 679, 570
Sakamoto, T., Barthelmy, S. D., Barbier, L., et al. 2008b, ApJS, 175, 179
Salvaterra, R., Della Valle, M., Campana, S., et al. 2009, Nature, 461, 1258
Schmidt, B. P., Suntzeff, N. B., Phillips, M. M., et al. 1998, ApJ, 507, 46
Shahmoradi, A., & Nemiroff, R. J. 2011, MNRAS, 411, 1843
Spergel, D. N., Bean, R., Doré, O., et al. 2007, ApJS, 170, 377
Tanvir, N. R., Fox, D. B., Levan, A. J., et al. 2009, Nature, 461, 1254
Ulanov, M. V., Golenetskii, S. V., Frederiks, D. D., et al. 2005, Nuovo Cimento C, 28, 351
Wang, F. Y., Dai, Z. G., & Liang, E. W. 2015, New Astron. Rev., 67, 1
Wang, J. S., Wang, F. Y., Cheng, K. S., & Dai, Z. G. 2016, A&A, 585, A68